ACS APPLIED MATERIALS & INTERFACES

Research Article

www.acsami.org

Controlled Electrochemical Etching of Nanoporous Si Anodes and Its Discharge Behavior in Alkaline Si–Air Batteries

Dong-Won Park,[†,∥] Soeun Kim,[‡,∥] Joey D. Ocon,[‡,§] Graniel Harne A. Abrenica,[‡] Jae Kwang Lee,[†] and Jaeyoung Lee*[,†,‡]

[†]Ertl Center for Electrochemistry and Catalysis, Research Institute for Solar and Sustainable Energies (RISE), Gwangju Institute of Science and Technology (GIST), Gwangju 500-712 South Korea

[‡]Electrochemical Reaction & Technology Laboratory (ERTL), School of Environmental Science and Engineering, GIST, Gwangju 500-712, South Korea

[§]Laboratory of Electrochemical Engineering (LEE), Department of Chemical Engineering, College of Engineering, University of the Philippines Diliman, Quezon City 1101, Philippines

Supporting Information

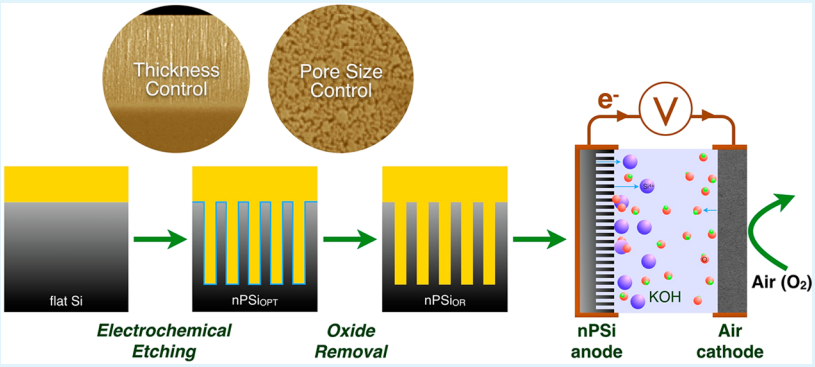

ABSTRACT: We report the fabrication of nanoporous silicon (nPSi) electrodes via electrochemical etching to form a porous Si layer with controllable thickness and pore size. Varying the etching time and ethanolic HF concentration results in different surface morphologies, with various degrees of electrolyte access depending on the pore characteristics. Optimizing the etching condition leads to well-developed nPSi electrodes, which have thick porous layers and smaller pore diameter and exhibit improved discharge behavior as anodes in alkaline Si–air cells in contrast to flat Si anode. Although electrochemical etching is effective in improving the interfacial characteristics of Si in terms of high surface area, we observed that mild anodization occurs and produces an oxide overlayer. We then show that this oxide layer in nPSi anodes can be effectively removed to produce an nPSi anode with good discharge behavior in an actual alkaline Si–air cell. In the future, the combination of high surface area nPSi anodes with nonaqueous electrolytes (e.g., room-temperature ionic liquid electrolyte) to minimize the strong passivation behavior and self-discharge in Si could lead to Si–air cells with a stable voltage profile and high anode utilization.

KEYWORDS: *nanoporous Si, electrochemical etching, ethanolic HF, semiconductor–air battery*

1. INTRODUCTION

Numerous studies have introduced new electrode materials and novel battery chemistries that are expected to go beyond the energy capacity and performance of the ubiquitous lithium-ion battery based on graphitic anodes. Particularly, metal–air batteries are considered as one of the most promising high-energy storage and conversion systems due to its high energy and power densities.[1−5] Despite the drawbacks related to the blockage of the cathode by oxide products (Li_2O and Li_2O_2) and safety issues associated with using lithium metal anodes, the lithium–air (Li–air) battery offers an excellent specific energy of 11 200 Wh kg^{-1}.[6−9] The above issues, however, including the corrosion and safety problems present in a Li–air battery under alkaline condition, represent scientific and technical obstacles before the potential of the Li–air battery can be realized. Recently, silicon (Si) was introduced as an attractive anode for metal–air batteries due to its relative abundance, low cost, and safety of use.[10,11] A silicon–air (Si–air) battery has a very high energy capacity of 3822 mAh g^{-1} via a four-electron oxidation reaction, which is comparable to that of a Li–air battery (3860 mAh g^{-1}).[12−14] Furthermore, use of semiconductor Si anodes could surmount the safety and cost issues encountered in Li metal-based Li–air batteries.

Received: October 23, 2014
Accepted: January 16, 2015
Published: January 16, 2015

DOI: 10.1021/am507360e
ACS Appl. Mater. Interfaces 2015, 7, 3126−3132

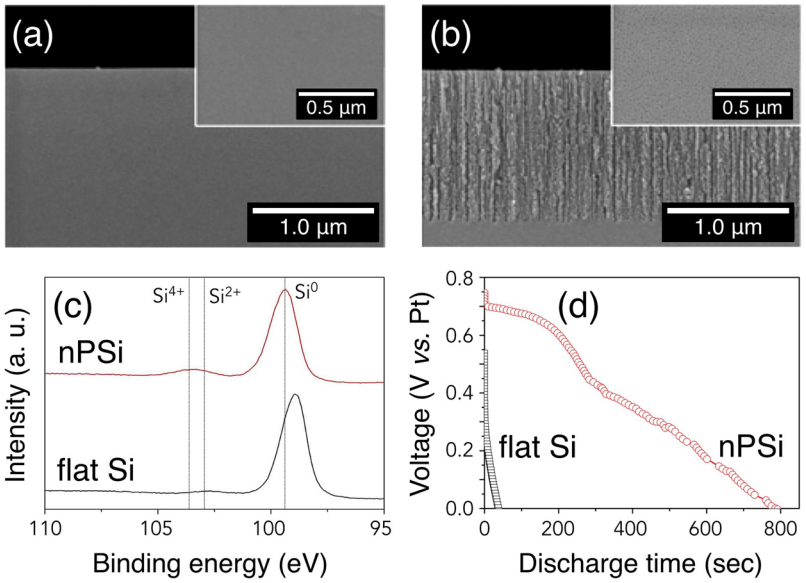

Figure 1. Cross-sectional and top-view SEM images of (a) a flat Si electrode and (b) an electrochemically etched nPSi electrode. (c) Si 2p X-ray core level photoelectron spectra of a flat Si electrode and an electrochemically etched nPSi electrode. (d) Galvanostatic discharge curves of a flat Si electrode and an electrochemically etched nPSi electrode. The half-cell test was operated at a discharge current density of 5 μA cm^{-2}.

Semiconductor−air batteries were introduced as a more accurate term to denote metal−air batteries that use semiconductor anodes, such as Si and Ge.[5] These semiconductor−air batteries mostly use aqueous alkaline electrolyte because it has good ionic conduction and can facilitate the reduction of oxygen.[4,5,18,19] In the case of Si anodes, however, the battery exhibits rapid potential drop mainly due to the fast passivation of the Si surface in alkaline solutions, terminating the discharge and severely limiting the usable energy.[5] For instance, Y. Ein-Eli et al. used a room-temperature ionic liquid (RTIL)-based primary Si−air battery in order to solve the passivation and self-corrosion phenomena.[16,17] Although this approach has been successful, additional costs and severe chemical safety issues are introduced because of the use of these fluoride-based RTIL electrolytes. Another group proposed a Si−air battery using nanostructured porous silicon fabricated by metal-assisted electroless etching and an alkaline-based electrolyte.[18] Recently, a thin-film flexible Si−air battery, using an n-doped amorphous Si anode and low concentrated alkaline electrolyte, has been demonstrated.[19]

Despite the many developments, there is a plethora of issues that are yet to be solved. A key approach to improving the discharge behavior of semiconductor anodes is the use of high surface area electrodes, as exhibited in few studies on Si and Ge.[4,18] For example, porous Si has drawn significant attention as an electrode material, especially in Li-ion batteries, due to its excellent mechanical and thermal properties and low cost. Furthermore, it has a high surface area, controllable pore size and thickness, and convenient surface chemistry in aqueous solutions.[20] Porous Si exhibits rich morphological features resulting from a set of very complex reaction processes at the Si/electrolyte interface.[21−23] It has been established that the most important parameters, which control the characteristics of porous Si obtained by electrochemical etching, are the composition and concentration of the hydrofluoric acid (HF)-containing electrolyte, current density, and etch duration.[24,25]

In this paper, we describe the formation of nanoporous silicon structure with different pore diameter and thickness. Different surface morphologies with unique interfacial features were obtained through the manipulation of etching parameters (i.e., etching time and ethanolic HF concentration). We then show and explain its behavior as a negative electrode in an actual semiconductor−air battery, which employs an aqueous alkaline electrolyte.

2. EXPERIMENTAL SECTION

The silicon wafers used in this work are p-type, boron-doped Si with (100) orientation and a resistivity of <0.005 Ω cm (MTI Corp.). Large Si wafers (4 in diameter) were cleaved into smaller cuts, with an approximate area of 1 cm^2. First, the Si wafers were immersed into 20 wt % HF (Sigma-Aldrich) to remove the native oxide layer. Then, the Si wafers were rinsed with deionized (DI) water and dried using a nitrogen flow gun. Electrochemical etching of the Si wafers was performed under anodic bias in HF-based electrolytes. In the electrochemical etching cell, the Si wafer was used as the working electrode and an oxidative (positive) current or potential was applied to initiate the etching process. Specifically, we used ethanolic HF solution in which an ethanol solution was added to an HF solution to improve the uniform formation of porous Si layers (Figures S1 and S2, Supporting Information). The hydrogen bubbles generated during etching were removed by mechanical stirring. In a typical etching experiment, a Si wafer was placed in a Teflon etching cell with ethanolic HF solutions (3.0, 5.0, and 15.0 wt %) of different concentrations. All etching experiments were performed at room temperature (without illumination) and controlled using a potentiostat/galvanostat (VSP, Biologic) with a power source (Keithley 2400) at the selected current density or voltage. Afterward, the samples were rinsed with ethanol and air dried to prevent cracking caused by the large capillary stress.

The surface morphology of porous Si layers was investigated using a field-emission scanning electron microscope (FE-SEM; Hitachi, S-4700) in plain and cross-sectional views. X-ray diffraction (XRD) measurements were performed using an automatic X-ray diffractometer (Rigaku, Miniflex II). The surface oxide coverage was investigated using lab-based X-ray photoelectron spectroscopy equipment (XPS, Thermo VG Scientific, MultiLab 2000) with an Mg Kα X-ray source (1253.6 eV) at a base pressure of 2 × 10^{-9} Torr and a synchrotron-based XPS beamline at the Pohang Light Source (PLS). In the latter,

DOI: 10.1021/am507360e
ACS Appl. Mater. Interfaces 2015, 7, 3126−3132

the applied photon energy was set to 630 eV, and the binding energies of the spectra were calibrated using the peak position of Au 4f (85.98 eV).

In galvanostatic discharge measurements, flat p-type Si and nanoporous p-type Si (nPSi) wafers were used as working electrodes in a 0.1 M potassium hydroxide (KOH) electrolyte with platinum wire as the reference and counter electrode in a multichannel high performance battery tester (Maccor 4300 K) at the selected current density. Subsequently, to test the full cell discharge behavior of Si anodes, a semiconductor–air cell—consisting of nPSi anodes, KOH electrolyte, platinum on carbon (Pt/C) cathode, and thin copper (Cu) meshes as current collectors—was assembled. The air-breathing cathode was fabricated by spraying a mixture of 46.7 wt % Pt/C (Tanaka, 1.0 mg cm^{-2}) and Nafion solution (Sigma-Aldrich, 10 wt %) on a gas diffusion layer (SGL, 25AA). All cells were assembled and operated under ambient conditions at various current drains.

3. RESULTS AND DISCUSSION

3.1. Characteristics of the Electrochemically Etched Nanoporous Si (nPSi). Figure 1a and 1b shows the cross-sectional and top-view scanning electron microscopy (SEM) images of flat Si and nPSi samples, respectively. As mentioned above, the etching rate and morphological evolution of the etched layer strongly depend on the applied current density and etchant concentration. For example, the porous layer (PL) formed by electrochemical etching at a current density of 1.0 mA cm^{-2} in 5.0 wt % ethanolic HF solution for 30 min had an approximate thickness of 1.5 μm and a pore diameter of 20 nm. Undoubtedly, these cylindrical-like pores allow more penetration of electrolyte, which could generate a larger surface area as the etching progresses.

To confirm the possible bulk crystallinity changes in Si wafer after etching, X-ray diffraction (XRD) measurements were carried out. As shown in Figure S3, Supporting Information, there are no significant differences in the XRD pattern of flat Si and nPSi. In both samples, the sharp peaks at 33.2° and 69°, corresponding to Si(200) and Si(400) diffraction planes, respectively, were observed. Similar to etched Ge wafers, no bulk crystallinity changes occurred despite long-time etching.[4]

In addition, X-ray photoelectron spectroscopy (XPS) was performed to observe the surface composition of the electrodes before and after electrochemical etching. Figure 1c shows the Si 2p XP spectra obtained from flat Si and nPSi samples. Each spectrum has two distinct peaks that are readily attributable to the elemental Si (98–100 eV) and the thin SiO_2 layer (103–104 eV).[13] In nPSi, the elemental Si peak was slightly shifted to higher binding energy (BE). Furthermore, the peak intensity of SiO_2 was noticeably enriched when compared with the SiO_2 peak in flat Si. Generally, the higher BE peaks usually corresponding to SiO_2 are split into a low BE peak (102–102.5 eV) corresponding to SiO_x or Si–O–F bonds and a high BE peak (103.5 eV) corresponding to Si–O bonds.[14,26] Nevertheless, the low intensity of the high BE peak confirmed that little oxide remained on the surface of nPSi after etching at a current density of 1.0 mA cm^{-2} in 5.0 wt % ethanolic HF. In fact, the existence of small amounts of silica on nPSi is helpful in making the surface more hydrophilic, which could facilitate diffusion of electrolyte into the pores easily.

The improved interfacial characteristics of nPSi are evident in its half-cell discharge behavior. The galvanostatic discharge curves of flat Si and nPSi at a discharge current density of 5 μA cm^{-2} are presented in Figure 1d. The voltage in flat Si electrode dropped immediately due to the strong passivation behavior in Si. In contrast, the nPSi electrode exhibited a sustained discharge, leading to a higher capacity of at least 60 times that of flat Si electrode. Thus, it is expected that well-designed nanoporous structures via control of etching parameters could give rise to improved discharge behavior of Si anodes.

3.2. Influence of the Thickness of the Porous Layer and Pore Diameter on the Discharge Characteristics of nPSi Anodes. We also fabricated nPSi electrodes with different PL thickness and investigated its effect on the discharge behavior. By operating in galvanostatic control, various nPSi electrodes of different PL thickness can be prepared as a function of the etching time. The current–voltage (I–V) curve during electrochemical etching of Si at 5.0 wt % ethanolic HF (Figure S4, Supporting Information) shows an analogous behavior to the commonly observed I–V curve in Si/HF systems.[27] It consists of three well-defined regions: a porous Si formation region, a transition region, and an electropolishing-dominated region.[20,25] We found that the onset current density of electropolishing is at around 1.8 mA cm^{-2}, while an etching current density of 1.0 mA cm^{-2} results in a more uniform PL formation. With the critical current density of 1.0 mA cm^{-2}, different thickness of the PL was obtained by etching in 5.0 wt % ethanolic HF at various etching times.

Figure 2 displays the SEM images of nPSi electrodes obtained at various etching times of 0.5, 1, 2, and 3 h. The cross-sectional SEM images in the right-hand side show uniform vertical arrays of nPSi, with a nearly constant diameter of around 20 nm except for the 3 h sample where etch pits existed. As expected, the PL thickness in nPSi increased from 1.5 to 8.5 μm with etching time. Furthermore, the surface of nPSi became rougher as etching progresses, as seen in the left-hand side figures in Figure 2. Evidently, dissolution of the

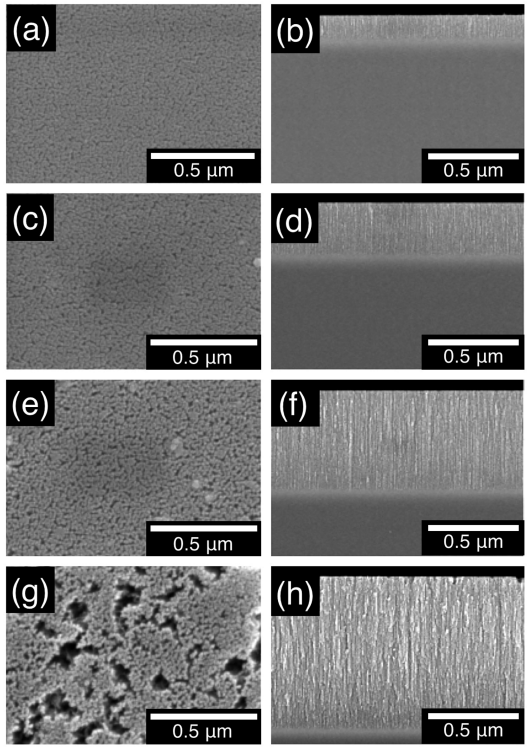

Figure 2. Cross-sectional and top-view SEM images of nPSi electrodes formed in 5.0 wt % ethanolic HF solutions at various etching times: 0.5 (a, b), 1 (c, d), 2 (e, f), and 3 h (g, h).

DOI: 10.1021/am507360e
ACS Appl. Mater. Interfaces 2015, 7, 3126–3132

already-formed PL occurred during long-time etching leading to a lower etching rate, a phenomenon similarly observed in Si etching in aqueous HF solutions.[20]

The galvanostatic half-cell discharge profiles of nPSi electrodes with different thickness in 0.1 M KOH electrolyte are shown in Figure 3. Increasing the nPSi thickness resulted in

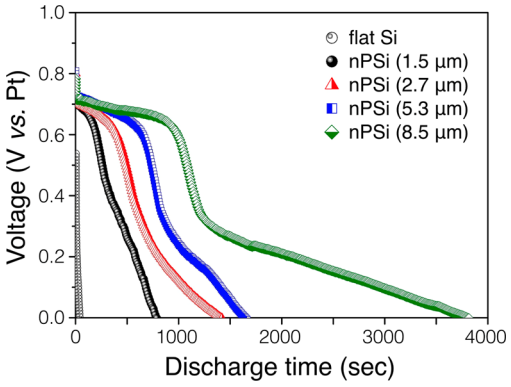

Figure 3. Galvanostatic discharge curves of nPSi anodes with various thicknesses in 0.1 M KOH electrolyte. The half-cell test was operated at a discharge current density of 5 μA cm^{-2}.

longer discharge and higher energy capacity. In addition, the drastic voltage drop observed in flat Si anode was not observed in nPSi, especially the nPSi anode with the thickest PL (8.5 μm). The capacity values obtained for the nPSi electrode discharges are approximately 0.41, 0.66, 0.96, and 1.61 mWh cm^{-2} for different thickness of 1.5, 2.7, 5.3, and 8.5 μm, respectively. The cell energy capacity is linearly proportional to the thickness of the PL, with an R^2 value of 0.987. It is apparent that the increased surface area allows more interaction between the electrolyte and the elemental Si surface.

Galvanostatic discharge curves of alkaline Si–air cells have different shapes, with an initial stable part and tail part after the voltage drop. To understand this behavior, the reactions that occur in the anode during discharge should be considered.[18]

$$\text{Si oxidation reaction: } Si_{(s)} + 4OH^- \rightarrow Si(OH)_4 + 4e^- \quad (1)$$

$$\text{Surface passivation: } Si(OH)_4 \rightarrow SiO_{2(s)} + 2H_2O \quad (2)$$

Initially, nPSi reacts with hydroxide ions to generate $Si(OH)_4$. It is believed that the two separate regions were caused by the difference in surface area. More reactions happen due to the higher surface area and the relatively strained nature of Si–Si bonds in nPSi anodes.[27] While $Si(OH)_4$ is soluble in alkaline solutions, its slow dissolution coupled with fast anode oxidation kinetics could lead to passivation of the surface via oxide formation. Once the surface is passivated, the oxide layer blocks further oxidation reactions and makes the rest of the anode unusable. According to previous studies, however, deep-channeled nPSi has low utilization of the available active surface area due to the strong capillary action, resulting in limited electrolyte penetration.[28,29] Therefore, the initial discharge reaction most likely takes place at the limited region where electrolyte access is allowed.[30] This limits the usefulness of Si–air cells and requires the use of high surface area Si anodes for practical purposes. For instance, thicker nPSi electrodes have long and stable discharge profiles, with less abrupt potential drops during discharge.

For perfectly observing the effect of surface area, we also tried to control the pore diameter of nPSi to allow improved electrolyte access during discharge. In contrast to the uniform thickness control using constant current, we found that applying a constant potential in the etching process can control the pore diameter of nPSi. Specifically, we applied a constant potential of 0.25 V with different concentation of ethanolic HF solutions.

The SEM images of the nPSi electrodes with different pore sizes in the top and cross-sectional views are shown in Figure 4.

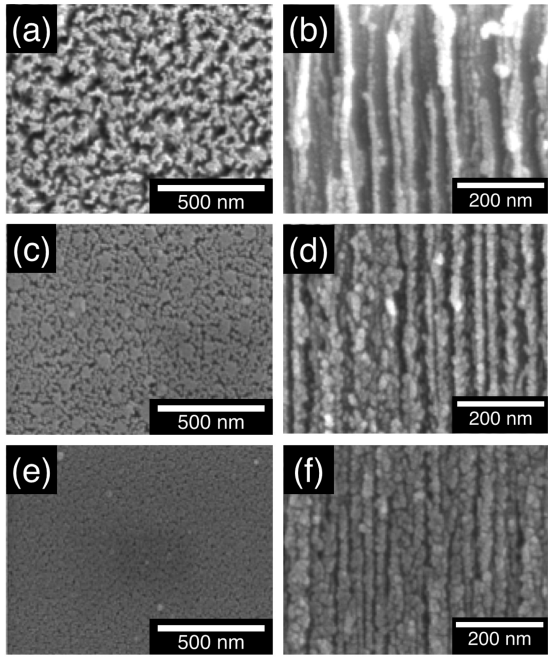

Figure 4. Cross-sectional and top-view SEM images of nPSi electrodes with different pore diameters obtained by etching in different concentrations of the etching solution: 3.0 (a, b), 5.0 (c, d), and 15.0 wt % ethanolic HF (e, f).

These nPSi electrodes were electrochemically etched in different concentrations of ethanolic HF (3, 5, and 15 wt %), and the PL thickness was controlled to 1.5 μm for all samples. To fabricate the same thickness, the nPSi samples were etched for 30, 20, and 5 min in 3, 5, and 15 wt % ethanolic HF, respectively. Higher concentration of etching solution facilitates a faster etching rate, resulting in a deeper PL with the same etching duration. As seen in Figure 4, increasing the ethanolic HF concentration led to a more compact PL with smaller pore sizes. It is assumed that a slower etching rate creates large primary defects at the onset of etching. Continuous etching arises from these defects formed. Eventually, larger defects from lower concentrations of the etching solutions make larger pore diameter.

To study the impact of pore diameter on the half-cell discharge behavior, galvanostatic discharge experiments were carried out using nPSi anodes with different pore sizes in 0.1 M KOH electrolyte, Figure 5. The nPSi anode with the smallest pore diameter of around 10 nm exhibited the best flat discharge behavior without an abrupt drop in operating voltage. On the contrary, the nPSi anode with the largest pore size demonstrated a sharp potential drop and low energy capacity. Similar to the effect of PL thickness, the surface area increases with decreasing pore diameter, allowing for more Si oxidation

DOI: 10.1021/am507360e
ACS Appl. Mater. Interfaces 2015, 7, 3126–3132

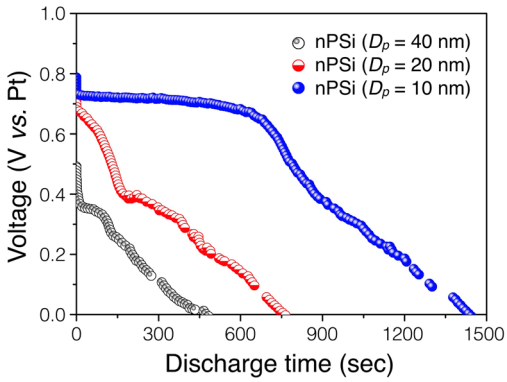

Figure 5. Galvanostatic discharge curves of nPSi anodes with various pore diameters in 0.1 M KOH electrolyte. The half-cell test was operated at a discharge current density of 5 μA cm^{-2}.

sites and preventing fast passivation. The energy capacities obtained for the nPSi anodes are 0.97, 0.34, and 0.12 mWh cm^{-2} for samples with diameters of 10, 20, and 40 nm, respectively. Interestingly, this result shows that the discharge capacity values are more affected by the pore diameter than that of PL thickness.

As demonstrated in the results above, we found that thicker PL and smaller pore sizes could lead to sustained Si discharge and higher discharge capacity. To further enhance the discharge capacity, we extended the etching time of the condition that could lead to a pore diameter of 10 nm to generate an nPSi electrode with thicker PL. Beyond an etching time of 2 h, however, severe dissolution of the already formed PL was observed. As shown in the inset SEM image in Figure 6, the

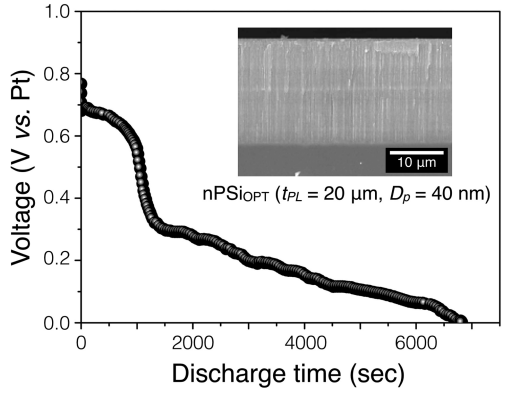

Figure 6. Galvanostatic discharge curve of the optimized nanoporous Si (nPSi$_{OPT}$) anode formed in 15 wt % ethanolic HF for 2 h. The half-cell test was operated at a discharge current density of 5 μA cm^{-2}.

optimized nPSi (nPSi$_{OPT}$) electrode has a uniform thickness of around 20 μm and a pore diameter of 10 nm. In the galvanostatic half-cell discharge test, an initial stable voltage of around 0.68 V was observed and then the voltage gradually lowered with time. Although the discharge–potential profile showed a roughly similar tendency with the discharge curves in Figure 3, the nPSi anode represents a higher capacity of 2.11 mWh cm^{-2}, which is 2.2 times that of only diameter-controlled nPSi anode and over 1.3 times that of only thickness-controlled nPSi anode.

To demonstate that the nPSi anodes are highly applicable in actual semiconductor–air cells, we assembled a Si–air device (Figure S5, Supporting Information) consisting of the nPSi as anode, aqueous KOH as electrolyte, and 46.7 wt % Pt/C as cathode. Pt/C was used as the oxygen reduction reaction catalyst in order to make sure that the anode will mainly dictate the discharge performance. As seen in Figure 7a, the nPSi$_{OPT}$

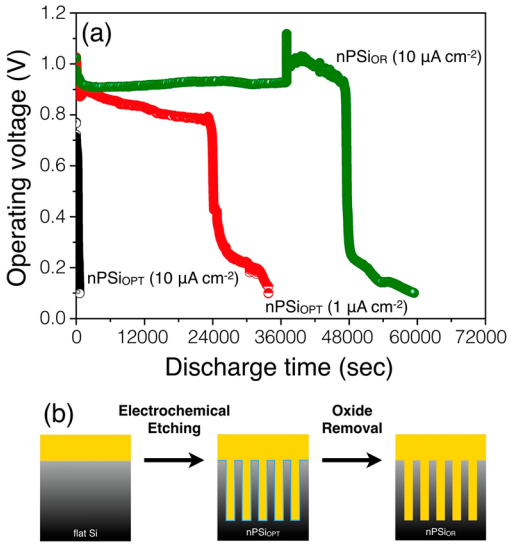

Figure 7. (a) Galvanostatic discharge profiles of nPSi anodes in actual Si–air cells. Both nPSi$_{OPT}$ anodes were discharged in 1.0 M KOH electrolyte at two current drains (1 and 10 μA cm^{-2}). Meanwhile, the oxide-removed nanoporous Si (nPSi$_{OR}$) anode was discharged in 6.0 M KOH electrolyte at a current density of 10 μA cm^{-2}. (b) Schematic illustration of the nPSi formation with anodization and the proposed extra oxide-removal step to maximize the available surface reactions sites in the nPSi anodes for higher operating voltage and energy capacity utilization.

anode operated better at the lower current density of 1 μA cm^{-2}, having a flat discharge potential (~0.8 V) for 24 000 s of operation. On the other hand, the nPSi$_{OPT}$ anode discharged at 10 μA cm^{-2} operated only up 600 s. We surmise that this is due to the mild anodization of the Si substrate during electrochemical etching to produce the nPSi$_{OPT}$ electrode. This is evident in the enrichment of the SiO_2 peak in the Si 2p X-ray photoelectron spectrum of the nPSi$_{OPT}$ sample in contrast to the elemental Si-rich flat Si sample (Figure S6, Supporting Information). The high oxide coverage in nPSi$_{OPT}$ is detrimental when the Si–air cell is operated at high current densities due to the amplified surface passivation. Hence, we added an extra oxide removal step after the etching process to derive an oxide-removed nPSi (nPSi$_{OR}$) by continuously exposing the nPSi to a highly concentrated 48.0 wt % HF solution, as described in the scheme in Figure 7b. The discharge performance of nPSi$_{OR}$ anode improved considerably even at a current density of 10 μA cm^{-2}, having a stable voltage above 0.9 V up to 48 000 s of operation. The higher concentration of KOH electrolyte is also critical in dissolving the discharge products, $Si(OH)_4$, to prevent fast oxide formation. For these reasons it is believed that both the surface area and the oxide coverage are crucial in improving the performance of nPSi anodes. In combination with nonaqueous electrolytes (e.g., room-temperature ionic liquid) that could minimize the surface passivation and self-discharge, Si–air batteries using high surface area nPSi anodes could power specific applications in the future.

DOI: 10.1021/am507360e
ACS Appl. Mater. Interfaces 2015, 7, 3126–3132

4. CONCLUSIONS

Our results indicate that the discharge performance of p-type Si anodes can be improved by fabricating a nanoporous layer via controlled electrochemical etching. In pore formation, the thickness of the PL is mainly determined by the etch duration while the pore size is strongly dependent on the concentration of the ethanolic HF etchant solutions. Having thicker PL and smaller pore diameter result in improved discharge capacity due to the increased surface area for the multielectron Si oxidation. Moreover, the etching process can be optimized to generate well-developed nPSi electrodes, having thick PL and small pore sizes. Although electrochemical etching is successful in increasing the surface area of Si, we observed that mild anodization occurs and the surface oxide coverage is enhanced. Nevertheless, this oxide layer in nPSi anodes can be effectively removed to produce an nPSi anode with good discharge behavior in an actual alkaline Si−air cell. In the future, the combination of high surface area nPSi anodes with nonaqueous electrolytes (e.g., room-temperature ionic liquid electrolyte) to minimize the strong passivation behavior and self-discharge in Si could lead to Si−air cells with a stable voltage profile and high anode utilization.[14,16,17] An extended inquiry should also investigate the use amorphous porous Si anodes, which might be able to slow the passivation phenomenon, or applying nPSi electrodes in high-temperature rechargeable Si−air batteries.[19,31]

■ ASSOCIATED CONTENT

Ⓢ Supporting Information

Effect of ethanol in the electrochemical etching of Si in HF; cross-sectional SEM images of PSi electrodes produced in HF and EtOH−HF solutions; XRD profiles of flat Si electrode and nPSi electrode; characteristic *I*−*V* curve of the electrochemical etching of Si in EtOH−HF solutions and representative SEM images at different etching conditions, Si 2p XP spectra of flat Si anode and $nPSi_{OPT}$ anode; schematic diagram of the Si−air cell architecture used in evaluating the discharge behavior of nPSi anodes and photograph of the actual Si−air cell. This material is available free of charge via the Internet at http://pubs.acs.org.

■ AUTHOR INFORMATION

Corresponding Author

*Tel.: +82 62 715 2434. Fax: +82 62 715 2571. E-mail: jaeyoung@gist.ac.kr.

Author Contributions

‖These authors contributed equally to this work.

Notes

The authors declare no competing financial interest.

■ ACKNOWLEDGMENTS

This work was supported by the Core Technology Development Program for Next-generation All-Solid Battery of KITECH. The authors gratefully acknowledge the authorities concerned at the Pohang Light Source (P.L.S.) for the use of beamline 8A1 for XPS measurements.

■ REFERENCES

(1) Abraham, K. M.; Jiang, Z. A Polymer Electrolyte-based Rechargeable Lithium/Oxygen Battery. *J. Electrochem. Soc.* **1996**, *143*, 1−5.

(2) Kraytsberg, A.; Ein-Eli, Y. Review on Li-air Batteries - Opportunities, Limitations and Perspective. *J. Power Sources* **2011**, *196*, 886−893.

(3) Hartmann, P.; Bender, C. L.; Vračar, M.; Dürr, A. K.; Garsuch, A.; Janek, J.; Adelhelm, P. A Rechargeable Room-Temperature Sodium Superoxide (Na_2O) Battery. *Nat. Mater.* **2013**, *12*, 228−232.

(4) Ocon, J. D.; Kim, J. W.; Uhm, S.; Mun, B. S.; Lee, J. An Etched Nanoporous Ge Anode in a Novel Metal-Air Energy Conversion Cell. *Phys. Chem. Chem. Phys.* **2013**, *15*, 6333−6338.

(5) Ocon, J. D.; Kim, J. W.; Abrenica, G. H. A.; Lee, J. K.; Lee, J. Quasi-Perpetual Discharge Behaviour in P-type Ge-air Batteries. *Phys. Chem. Chem. Phys.* **2014**, *16*, 22487−22494.

(6) Girishkumar, G.; McCloskey, B.; Luntz, A. C.; Swanson, S.; Wilcke, W. Lithium-Air Battery: Promise and Challenges. *J. Phys. Chem. Lett.* **2010**, *1*, 2193−2203.

(7) Lee, J. S.; Kim, S. T.; Cao, R. G.; Choi, N. S.; Liu, M.; Lee, K. T.; Cho, J. Metal-Air Batteries with High Energy Density: Li-Air versus Zn-Air. *Adv. Energy Mater.* **2011**, *1*, 34−50.

(8) Armand, M.; Tarascon, J. M. Building Better Batteries. *Nature* **2008**, *451*, 652−657.

(9) Park, D.-W.; Kim, J. W.; Kim, J.; Lee, J. Physicochemical Behaviors of Oxygen and Sulfur in Li Batteries. *Appl. Chem. Eng.* **2012**, *23*, 247−252.

(10) Winter, M.; Besenhard, J. O.; Spahr, M. E.; Novák, P. Insertion Electrode Materials for Rechargeable Lithium Batteries. *Adv. Mater.* **1998**, *10*, 725−763.

(11) Chan, C. K.; Peng, H.; Liu, G.; McIlwrath, K.; Zhang, X. F.; Huggins, R. A.; Cui, Y. High Performance Lithium Battery Anodes Using Silicon Nanowires. *Nat. Nanotechnol.* **2008**, *3*, 31−35.

(12) Adams, B. D.; Radtke, C.; Black, R.; Trudeau, M. L.; Zaghib, K.; Nazar, L. F. Current Density Dependence of Peroxide Formation in the Li-O_2 Battery and its Effect on Charge. *Energy Environ. Sci.* **2013**, *6*, 1772−1778.

(13) Freunberger, S. A.; Chen, Y.; Peng, Z.; Griffin, J. M.; Hardwick, L. J.; Bardé, F.; Novák, P.; Bruce, P. G. Reactions in the Rechargeable Lithium-O_2 Battery with Alkyl Carbonate Electrolytes. *J. Am. Chem. Soc.* **2011**, *133*, 8040−8047.

(14) Cohn, G.; Macdonald, D. D.; Ein-Eli, Y. Remarkable Impact of Water on the Discharge Performance of a Silicon-Air Battery. *ChemSusChem* **2011**, *4*, 1124−1129.

(15) Lown, D. A.; Thirsk, H. R. Proton Transfer Conductance in Aqueous Solution. Part 1. - Conductance of Concentrated Aqueous Alkali Metal Hydroxide Solutions at Elevated Temperatures and Pressures. *Trans. Faraday Soc.* **1971**, *67*, 132−148.

(16) Cohn, G.; Starosvetsky, D.; Hagiwara, R.; Macdonald, D. D.; Ein-Eli, Y. Silicon-Air Batteries. *Electrochem. Commun.* **2009**, *11*, 1916−1918.

(17) Cohn, G.; Ein-Eli, Y. Study and Development of Non-Aqueous Silicon-Air Battery. *J. Power Sources* **2010**, *195*, 4963−4970.

(18) Zhong, X.; Zhang, H.; Liu, Y.; Bai, J.; Liao, L.; Huang, Y.; Duan, X. High-Capacity Silicon-Air Battery in Alkaline Solution. *ChemSusChem* **2012**, *5*, 177−180.

(19) Garamoun, A.; Schubert, M. B.; Werner, J. Thin-Film Silicon for Flexible Metal-air Batteries. *ChemSusChem* **2014**, in press, DOI: 10.1002/cssc.201402463.

(20) Smith, R. L.; Collins, S. D. Porous Silicon Formation Mechanisms. *J. Appl. Phys.* **1992**, *71*, R1−R22.

(21) Steiner, P.; Lang, W. Micromachining Applications of Porous Silicon. *Thin Solid Films* **1995**, *255*, 52−58.

(22) Parkhutik, V. Porous Silicon − Mechanisms of Growth and Applications. *Solid-State Electron.* **1999**, *43*, 1121−1141.

(23) Ouyang, H.; Christophersen, M.; Viard, R.; Miller, B. L.; Fauchet, P. M. Macroporous Silicon Sensor Arrays for Chemical and Biological Detection. *Adv. Funct. Mater.* **2005**, *15*, 1851−1859.

(24) Bomchil, G.; Halimaoui, A.; Herino, R. Porous Silicon: The Material and its Applications to Silicon-on-Insulator Technologies. *Appl. Surf. Sci.* **1989**, *41*−*42*, 604−613.

(25) Zhang, X. G. Morphology and Formation Mechanisms of Porous Silicon. *J. Electrochem. Soc.* **2004**, *151*, C69−C80.

DOI: 10.1021/am507360e
ACS Appl. Mater. Interfaces 2015, 7, 3126−3132

(26) Czuprynski, P.; Joubert, O. X-ray Photoelectron Spectroscopy Analyses of Silicon Dioxide Contact Holes Etched in a Magnetically Enhanced Reactive Ion Etching Reactor. *J. Vac. Sci. Technol. B* **1998**, *16*, 1051−1058.
(27) Sailor, M. J. *Porous Silicon in Practice: Preparation, Characterization and Applications*, 1st ed.; Wiley-VCH: Weinheim, 2012; pp 1−42.
(28) Halimaoui, A. Influence of Wettability on Anodic Bias Induced Electroluminescence in Porous Silicon. *Appl. Phys. Lett.* **1993**, *63*, 1264−1266.
(29) Halimaoui, A. Determination of the Specific Surface Area of Porous Silicon from its Etch Rate in HF Solutions. *Surf. Sci. Lett.* **1994**, *306*, L550−L554.
(30) Shin, H.-C.; Corno, J. A.; Gole, J. L.; Liu, M. Porous Silicon Negative Electrodes for Rechargeable Lithium Batteries. *J. Power Sources* **2005**, *139*, 314−320.
(31) Inoishi, A.; Sakai, T.; Ju, Y.-W.; Ida, S.; Ishihara, T. A Rechargeable Si-Air Solid State Oxygen Shuttle Battery Incorporating an Oxide Ion Conductor. *J. Mater. Chem. A* **2013**, *1*, 15212−15215.

DOI: 10.1021/am507360e
ACS Appl. Mater. Interfaces 2015, 7, 3126−3132